

Hot Ground State Cooling Following Ultrafast Photoisomerization: Time-Resolved Infrared Spectroscopy

James N. Bull,* Mark H. Stockett,* Pratip Chakraborty, Eleanor K. Ashworth, Anam Fatima, Vincent J. Esposito, Gregory M. Greetham, Partha Malakar, and Stephen R. Meech




Cite This: <https://doi.org/10.1021/acs.jpcb.5c07581>



Read Online

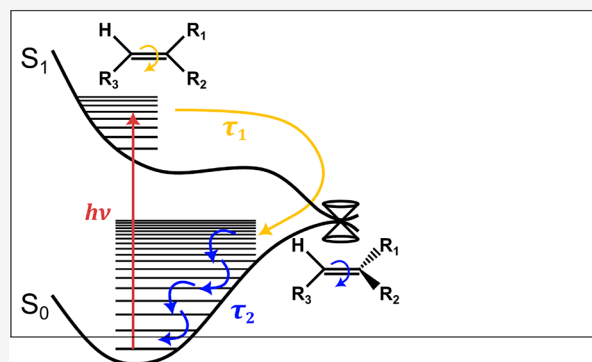
ACCESS |

 Metrics & More

 Article Recommendations

 Supporting Information

ABSTRACT: The ultrafast photophysics of many isomerizing molecules involves subpicosecond formation of a twisted hot ground state, which transfers energy to the environment through vibrational relaxation (cooling) over several picoseconds. In time-resolved infrared (TR-IR) spectroscopy, hot ground state transients show frequency shifts and band reshaping, which cannot be described through kinetic models that assume static spectral functions. We report a simple anharmonic cascade framework, which uses a single adjustable parameter associated with scaling the probability of vibrational energy transfer to the environment, for describing hot ground state cooling (HGSC) in TR-IR spectroscopy. The model is demonstrated against measurements on the cyan fluorescent protein chromophore. To best describe HGSC band shape evolution, the model utilizes *ab initio* data on anharmonic vibrational structure and nonadiabatic molecular dynamics trajectories of $S_1 \rightarrow S_0$ internal conversion for realistic vibration occupation numbers of the nascent hot ground state. The modeling framework is readily extended to include mode-specific rates for intermolecular energy transfer and can be applied to any ultrafast isomerizing molecule for which anharmonic vibrational properties can be computed.



INTRODUCTION

Ultrafast photoisomerization or molecular rotor motion of a double bond in a chromophore often occurs via passage through a conical intersection seam connecting the ground and first electronically excited state of the same spin multiplicity.¹ This is a widespread phenomenon, occurring throughout nature in mammalian vision² and photoactive proteins,^{3,4} in phototactic responses in light-sensitive bacteria,^{5,6} and in technological applications such as molecular photoswitches⁷ and photomolecular motors.^{8–11} Because *E-Z* (*trans-cis*) photoisomerizations usually involve substantial twisting about a double bond (azobenzenes may isomerize through inversions¹²), vibrational modes associated with the displacement become highly energized on formation of the twisted ground electronic state. In turn, it takes some picoseconds for all of intramolecular vibrational energy redistribution (IVR), intermolecular vibrational energy transfer (IET) to the environment, and geometric relaxation – collectively termed hot ground state cooling (HGSC) – to occur. In experiments based on ultrafast vibrational spectroscopy, HGSC transients contain averaged fingerprints of photoisomerization pathways. Notably, in time-resolved infrared (TR-IR) spectroscopy, HGSC signatures can be observed for energized vibrational modes, with their evolution linked to the nascent hot ground state geometries and nonequilibrium vibrational energy

distribution (Figure 1). In ultrafast TR-IR, because HGSC for the highly energized vibrational modes manifest as an evolving spectral profile with time (reshaping toward higher wavenumber), global fit models that assume static spectral basis functions are unable to provide physically meaningful kinetics. This work develops a simple framework for predicting HGSC active modes and corresponding band evolution using data on internal conversion from nonadiabatic molecular dynamics trajectories, with the purpose of helping to interpret experimental TR-IR data.

The relaxation of vibrational energy from a nascent hot ground state molecule in solution subsumes two processes:^{13,14} (i) IVR, where a nonequilibrium distribution of vibrational energy becomes statistically redistributed among internal modes, and (ii) IET, where vibrational energy is dissipated into individual and collective vibrations of the solvent molecules. Low frequency modes are typically more efficient for IET, requiring IVR to access such modes that, in turn,

Received: November 5, 2025

Revised: November 22, 2025

Accepted: November 24, 2025

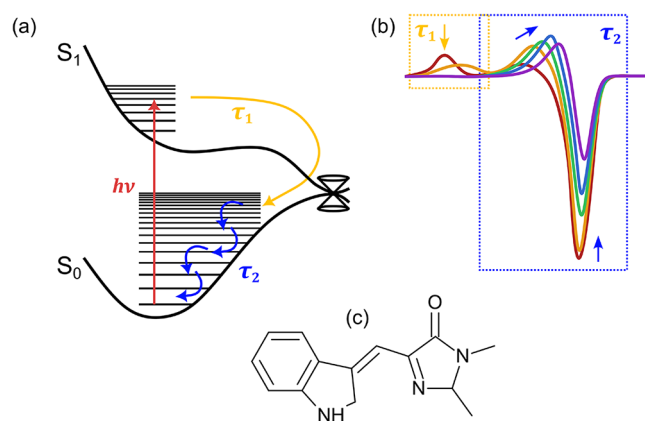


Figure 1. Hot ground state cooling (HGSC) dynamics in a photoisomerizing molecule involving S_0 and S_1 electronic states: (a) Potential energy surfaces for an ultrafast photoisomerization. Lifetime τ_1 is linked with loss of the S_1 state via passage through an isomerizing conical intersection seam, and lifetime τ_2 corresponds to HGSC. (b) Manifestation of these dynamics in ultrafast TR-IR spectra. The spectral shape and time-dependent reshaping of the HGSC profile for a given vibrational mode is defined by anharmonicity coefficients, the vibrational energy distribution, and vibrational energy relaxation processes. Note that the integrated ground-state bleach over a given band may be larger than the corresponding hot ground state absorption. (c) Cyan fluorescent protein chromophore (shown as the Z1 isomer).

efficiently transfer energy to solvent; these dynamics lead to complex solute- and solvent-dependent IET rates.^{15–18} The rates of IVR and IET have been well reviewed for small molecules (a few atoms) as they provide the clearest opportunities to elucidate microscopic analysis.^{13,15,19} For aromatic and conjugated molecules with 20 or more atoms and a spread of vibrational frequencies, IVR rates are usually a few picoseconds,^{20–22} such as for photoisomerizing Z-stilbene (sub-300 fs internal conversion) with a high degree of vibrational excitation over the mid-IR range.^{23–27} The implication is that IET and IVR occur on similar time scales need to be considered in concert and a HGSC model for ultrafast dynamics requires nonequilibrium vibration occupation numbers.

Preliminary foundations for describing HGSC have been considered by Shelby et al.²⁸ and Hamm et al.,²⁹ with the latter arguing the importance of an anharmonic approach. The limiting cases of ultrafast IVR, i.e., HGSC occurs from an equilibrated hot molecule (termed the rapid exchange limit in this work), and slow IVR with selective excitation of specific modes, were discussed in the latter. In other work, Murdock et al.³⁰ used first-order kinetics in a harmonic approximation to fit sigmoidal-like functions to HGSC bleach amplitudes in TR-IR spectra of thiophene carbonyl stretch modes.

We report a trajectory-based anharmonic cascade framework for describing HGSC in ultrafast photoisomerizing molecules, illustrated using the cyan fluorescent protein chromophore (Figure 1c, denoted cyan) dissolved in CD₃OD (deuterated methanol). Application of the HGSC framework requires input data on the (anharmonic) vibrations and expected vibration occupation numbers for the nascent hot ground state. The cyan chromophore is well suited for such a demonstration because: (i) The excited-state (S_1) lifetime is <500 fs, as determined by transient absorption and femtosecond fluorescence upconversion spectroscopies,³¹ with most electronic

energy rapidly converted into vibrational energy. (ii) There is a single internal conversion pathway involving Z–E twisting about a methylene double bond with a well-defined conical intersection seam with a photoisomerization quantum yield of a few percent in solution (meaning that analysis need consider only the synthesized Z isomer). (iii) Cyan is readily studied using ultrafast TR-IR spectroscopy in CD₃OD.³¹ While it is not possible to use such modeling to extract detailed anharmonic information from experimental TR-IR spectra, the model is useful for determining which modes might be active or displaced versus spectators in a photoisomerization mechanism, and for predicting HGSC band evolution in order to help interpret TR-IR spectra. For example, to help distinguish excited state absorption from HGSC in complex TR-IR spectra; this situation is particularly relevant for cyan and related fluorescent protein chromophores due to potential ambiguities in how many electronic excited states are involved in the ultrafast photophysics.³¹

METHODS

HGSC Model Framework. Our HGSC framework considers the total energy E , relative to the zero point energy, of a vibrational configuration $\mathbf{n} = (n_1, n_2, \dots, n_N)$, where N is the number of vibrational modes and n_i is the occupation number (quantum number) of mode i , in second-order vibrational perturbation theory (VPT2) as being given by the Dunham expansion:³²

$$E = \sum_i h\nu_i \left(n_i + \frac{1}{2} \right) + \sum_{i \leq j} X_{ij} \left(n_i + \frac{1}{2} \right) \left(n_j + \frac{1}{2} \right) \quad (1)$$

where ν_i is the frequency of mode i , and X_{ij} are elements of the anharmonic \mathbf{X} matrix (taken from electronic structure calculations described in the next section). The \mathbf{X} matrix contains anharmonic coupling constants between the fundamental vibrational modes, with diagonal terms describing self-anharmonicities and off-diagonal terms describing mode–mode couplings.

The fundamental band transition energies are

$$\Delta E_{\text{fund},i} = h\nu_i + X_{ii} \left(n_i + \frac{3}{2} \right) + \sum_{ij} X_{ij} \left(n_j + \frac{1}{2} \right) \quad (2)$$

Similar expressions for the first overtones and 1 + 1 combination bands are given in the Supporting Information. Note that we prefer n_i as a occupation (quantum) number rather than conventional ν_i in order to clearly distinguish from mode frequency, ν_i . The IR intensity of a fundamental band is

$$I_i = I_i^0 (n_i + 1) \left(\frac{\Delta E_{\text{fund},i}}{\Delta E_{\text{fund},i}^0} \right) \quad (3)$$

where the superscript 0 indicates the transition energy and intensity when $n_i = 0$ for all i (i.e., the default anharmonic values from a Gaussian VPT2 calculation). The scaling of the IR intensity with $n_i + 1$ is strictly valid for only the harmonic oscillator. Similar expressions for the first overtones and 1 + 1 combination bands are given in the Supporting Information.

The first step in obtaining the simulated IR spectrum at $T = 300$ K utilized a multicanonical (MUCA) sampling algorithm for the space of vibrational occupation numbers (i.e., giving the thermal occupation of each vibrational mode n_i at room temperature).^{33,34} The total energy range of interest (≈ 1 eV)

in the IR spectrum was divided into four nonoverlapping windows. For each window, a histogram \mathbf{H} with bin widths of 16 cm^{-1} was first set to zeros, as was a spectrum matrix with a row (spectrum) for each energy bin. Starting from the random sampled configuration \mathbf{n} , a new configuration \mathbf{n}_{prop} is proposed in which each n_i may decrease or increase by one quantum, subject to $n_i \geq 0$. The probability of proposing a downward step is $p_{\text{down}} = \frac{1}{N}$, while that of an upward step is $p_{\text{up}} = \frac{r}{N}$, where $r = 1.08$ was found to accelerate convergence. The proposed configuration was first validated by ensuring that the total energy (eq 1) remained in the window and that all fundamental transition energies obeyed $\Delta E_{\text{fund}} > 0$. Valid configurations were accepted with a probability given by a Metropolis-Hastings condition:³⁵

$$p_{\text{acc}} = \min \left[1, \frac{\rho(E)}{\rho(E_{\text{prop}})} r \Delta n \right] \quad (4)$$

where E and E_{prop} are the total energy of the current and proposed configurations, $\rho(E)$ is the density of vibrational states, and Δn is the difference in the total number of quanta between the current and proposed configurations. Here, the $\rho(E)$ was calculated using the Stein-Rabinovitch exact state counting algorithm,³⁶ treating the vibrations as separable anharmonic oscillators i.e., assuming $X_{i \neq j} = 0$. We note that published computations of fully coupled level densities using the Wang–Landau algorithm³⁷ have insignificant differences from uncoupled anharmonic calculations for $E < 1\text{ eV}$. If the proposed configuration is accepted, \mathbf{n}_{prop} replaces \mathbf{n} and E_{prop} replaces E . Regardless of acceptance, the energy bin of \mathbf{H} corresponding to E is incremented by 1. The transition energies and IR intensities for the fundamental, first overtone, and $1 + 1$ combination bands are computed for \mathbf{n} and the resulting spectrum is added to the row of the spectral matrix corresponding to the same energy bin. New steps are proposed until a flatness condition is met

$$\text{all} \left[\frac{\mathbf{H} - \langle \mathbf{H} \rangle}{\langle \mathbf{H} \rangle} < \alpha \right] \quad (5)$$

where $\langle \mathbf{H} \rangle$ is the mean value of \mathbf{H} , and $\alpha = 0.25$. Each row i of the spectral matrix is divided by the number of samples in the corresponding energy bin H_i . The final matrix is assembled from the four energy windows, each of which was sampled by six independent walks with different random initial configurations. This matrix contains the absorption spectrum associated with the microcanonical energy E corresponding to each row. To obtain the IR spectrum for a canonical temperature T , a weighted sum of the rows is performed, with the weights given by the Boltzmann distribution for that temperature.

Time-dependent IR spectra were simulated with a kinetic Monte Carlo approach that uses similar logic to the MUCA simulation. For cyan, two sets of simulations were performed: (i) projected vibration occupation numbers from nonadiabatic molecular dynamics (NAMD) trajectories, determined from surface-hopping geometries at the $S_1 \rightarrow S_0$ conical intersection seam (described in the NAMD Trajectories section), as the initial configurations; (ii) a set of random configurations yielding a similar distribution of initial total energies was generated – this corresponds to the rapid exchange limit for which IVR fully precedes IET. To each occupancy configuration, a randomly sampled configuration from a $T =$

300 K distribution \mathbf{n}_T was added to include the initial temperature of the system prior to excitation, giving initial configuration \mathbf{n} . The Monte Carlo trajectories evolved as follows. For each \mathbf{n} , a blank spectral matrix was initialized with a row for each time step ($dt = 5\text{ fs}$). The probability of proposing a downward step in n_i is $p_{\text{down},i} = q n_i \nu_i dt$, where $q = 0.1$ is an arbitrary scaling factor adjusted so that the time-evolution of the spectrum roughly matches that of the experiment – this is the single adjustable parameter in our HGSC model that affects only the rate, not the transient spectral shape. The probability of proposing an upward step, corresponding to energy gained from the bath, is $p_{\text{up},i} = q(n_i + 1) \nu_i dt \cdot e^{-h\nu_i/k_B T}$, where $T = 300\text{ K}$ is the temperature of the bath. We assume the isothermal bath approximation, where energy dissipation within the bath is sufficiently rapid so that the local bath temperature (first solvation shell of the molecule) is the same as the bulk bath temperature. The acceptance probability is $p_{\text{acc}} = e^{-(E - E_{\text{prop}})/k_B T}$. Unlike in the MUCA strategy above, configurations were not required to be within the valid range of the Dunham expression because some of the initial configurations given from NAMD projections are outside of these bounds and would never evolve. Negative transition energies are assigned zero intensity. Regardless of acceptance, the transition energies and IR intensities are calculated and stored in the row of the spectral matrix corresponding to the current time step. Many trajectories (576) were run for each initial configuration, and were averaged to construct the total time-dependent spectral matrix (from 46656 points).

Anharmonic Vibrational Properties. The spectral evolution and associated intensity changes of HGSC transients in TR-IR are largely governed by anharmonicity effects of highly excited vibrational modes, necessitating incorporation of fundamental bands, $1 + 1$ combination bands, first overtones, anharmonicity constants for each mode (e.g., \mathbf{X} matrix). For cyan, the anharmonic IR properties were computed via a quartic force field (QFF), which is a truncated fourth-order Taylor expansion of the potential portion of the Watson Hamiltonian, given by

$$V = \frac{1}{2} \sum_{i,j}^{3N} \left(\frac{\partial^2 V}{\partial X_i \partial X_j} \right) X_i X_j + \frac{1}{6} \sum_{i,j,k}^{3N} \left(\frac{\partial^3 V}{\partial X_i \partial X_j \partial X_k} \right) X_i X_j X_k + \frac{1}{24} \sum_{i,j,k,l}^{3N} \left(\frac{\partial^4 V}{\partial X_i \partial X_j \partial X_k \partial X_l} \right) X_i X_j X_k X_l \quad (6)$$

where X is a nuclear displacement. Optimized geometries, fundamental modes, and harmonic frequencies were determined at the B3LYP/N07D level of theory^{38,39} with Gaussian 16.C01.⁴⁰ These computations were performed using very tight optimization criteria (1×10^{-12}) and a custom integration grid consisting of 200 radial shells and 974 angular points per shell. The N07D basis set takes 6–31G and adds selected dispersion and polarization functions that improve the accuracy of calculated vibrational frequencies for large aromatic and highly conjugated molecules.⁴¹ Next, the normal coordinate QFF (quadratic, cubic, and semidiagonal quartic force constants) was computed using small displacements (0.01 Å steps) along all normal coordinates, with a linear transformation providing a Cartesian coordinate QFF.⁴² The vibrational spectrum was computed using second order vibrational perturbation theory (VPT2)^{43–45} within the

software program SPECTRO.⁴⁶ The VPT2 method implemented in SPECTRO utilizes a resonance polyad matrix approach.^{47–49} When two vibrational states of the same symmetry are close in frequency, they create a near-singularity in the conventional VPT2 equation. Here, the interacting states were removed from the VPT2 computation and were included in resonance polyad matrices based on symmetry. These matrices allow for the treatment of resonance effects while also accounting for states that simultaneously participate in multiple resonance interactions, termed resonance chaining. Additionally, the resonance polyads treat the redistribution of intensity between coupled states by using the eigenvectors of the diagonalized matrix.^{49,50} The maximum frequency separation for a resonance in the polyad treatment was set to 200 cm^{−1}.^{49,51} Our anharmonic computation strategy with SPECTRO typically produces (gas phase) frequencies with a mean absolute error between theory and gas-phase experiments of ≈ 5 cm^{−1}, and shows good agreement with (gas phase) experimental intensities – see refs 52,53, and references therein; harmonic approximation computations have poor agreement with experiment. While B3LYP is suitable for describing ground electronic states of main group organic at equilibrium geometries, it has well-known failures for excited states and particularly those with charge-transfer character or for excited-state geometries in the vicinity of a conical intersection.⁵⁴ Consequently, we determined harmonic and anharmonic frequencies using the BH&HLYP/N07D level of theory (where BH&HLYP has 50% Hartree–Fock exchange).⁵⁸ Harmonic frequencies were checked against MRSF-TDDFT values (described next) and were found to have little deviation.

NAMD Trajectories. NAMD dynamics on cyan were performed using MRSF-TDDFT⁵⁵ at the BH&HLYP/6–31G* level of theory⁵⁶ in GAMESS-US (July 2024 R2 release).⁵⁷ The NAMD trajectories used Tully's fewest-switches surface-hopping algorithm,⁵⁸ with nonadiabatic coupling vectors computed numerically using a fast overlap method.^{59,60} Velocity Verlet was used for integration. The trajectories were propagated for 1500 fs (1.5 ps) with a time step of 0.5 fs. Energy conservation during the hops was ensured by rescaling of the velocities. The nuclear degrees of freedom were propagated with a subtime-step size of 10^{−5} fs for the electronic degrees of freedom.^{61,62} No corrections for decoherence were applied. 110 trajectories were initiated on the S₁ state and 97 were included in the statistics (11 removed due to SCF convergence issues and backward hops because decoherence was not considered). We note that the same MRSF-TDDFT methodology has been benchmarked against CASSCF and XMS-CASPT2 potential energy surfaces for the related green fluorescent protein chromophore.^{62,63} The initial occupation numbers n_i after surface hopping were computed for each trajectory by projecting the equilibrium and surface hopping geometries with the (mass weighted) normal vectors for the equilibrium geometry, with the requirement that the electronic energy difference between the S₁ state at the hopping geometry and S₀ state equilibrium geometry is partitioned into fundamental modes. Because most of the 87 fundamental modes are spectators in the internal conversion process, only 14 modes gained substantial occupation in the projections. These 14 modes are those that would show HGSC dynamics reflective of the isomerization mechanism.

Initial geometries and velocities for the NAMD trajectories were obtained from ground state sampling at the BH&HLYP/6–31G* level of theory. This involved four ground-state

molecular dynamics trajectories that were propagated (≈ 0.48 fs steps) and thermalized with a quantum thermostat^{64,65} using the ABIN code⁶⁶ interfaced to Gaussian 16, initiated from the optimized geometry with velocities obtained from a Boltzmann distribution. The Generalized Langevin Equation (GLE) thermostat parameters (drift and diffusion matrices A and C) were collected from the GLE4MD webpage⁶⁷ for $T = 298.15$ K, along with $N_s = 6$ (additional degrees of freedom), $\hbar\omega_{\max}/k_B T = 20$, in the strong coupling regime. ω_{\max} represents the maximum fundamental mode frequency for which the GLE parameters were optimized, for a particular temperature. At $T = 298.15$ K, $\omega_{\max} = 4114.5$ cm^{−1}, which is larger than the highest frequency fundamental mode. Equilibration time of the trajectories was determined by monitoring the convergence of the average kinetic energy temperature.⁶⁸ The initial geometries and velocities for NAMD trajectories were obtained by taking snapshots at ≈ 100 fs intervals from the thermalized portion of the thermostat trajectories.

Experimental Section. Ultrafast TR-IR spectroscopy on cyan (1–2 mM in CD₃OD, $T = 293$ K) was performed using the ULTRA LifeTime system at the Central Laser Facility, Research Complex at Harwell, Rutherford Appleton Laboratory, UK.⁶⁹ The sample, in a 50 μ m path length CaF₂ cell, was excited with 400 nm light pulses (500 nJ, 150 μ m spot size) at a 1 kHz repetition rate, and probed with a delayed IR pulse to capture transient vibrational spectra (cross correlation ≈ 200 fs). The sample position was rastered in two dimensions during measurements to minimize localized photobleaching and degradation. Measurements were performed with and without the pump pulse (pump-on/pump-off) under magic angle polarization geometry. Spectral calibration used a standard polystyrene IR spectrum.

RESULTS AND DISCUSSION

The computed IR spectrum for (gas phase) cyan, shown in Figure 2a ($T = 0$ K, B3LYP/N07D VPT2 with resonance polyad mixing via SPECTRO)^{52,53} over the experimental TR-IR window (1350–1850 cm^{−1}). Over this window, the intensity arises from 62.8% fundamental modes, 33.8% combination bands (almost exclusively 1 + 1), and 3.4% first overtones. While empirical scaling of harmonic frequencies largely corrects for frequency differences,⁷⁰ it does not remedy inadequate band intensities for fundamental modes from the harmonic approximation. Furthermore, intensity deviations between VPT2 and the resonance polyad corrected spectrum,⁷¹ stemming from resonance and intensity sharing (notably, the intensity of carbonyl stretch mode ν_{14} is decreased), are sufficiently different to conclude that harmonic intensities are poor. The most pronounced mode, ν_{15} , corresponds to methylene bridge C=C stretching, and is flanked by two 1 + 1 combination bands ($\nu_{84} + \nu_{10}$ and $\nu_{59} + \nu_{49}$) and the only significant overtone (ν_{54}^2); the summed intensity for these three flanking vibrations exceeds that for ν_{15} . Mode ν_{19} is linked with C–C (single bond) stretching on the methylene bridge. A frequency scaling factor of 0.992 was required to best align our calculated anharmonic frequencies with the experimental spectrum in CD₃OD. The simulated spectrum for $T = 300$ K (gas phase) cyan using VPT2 data (but no resonance polyad mixing via SPECTRO) is shown in Figure 2b. There is good agreement over the ν_{15} region with the CD₃OD spectrum, although the ν_{14} (carbonyl stretch) region is particularly difficult to describe due to strong solute–

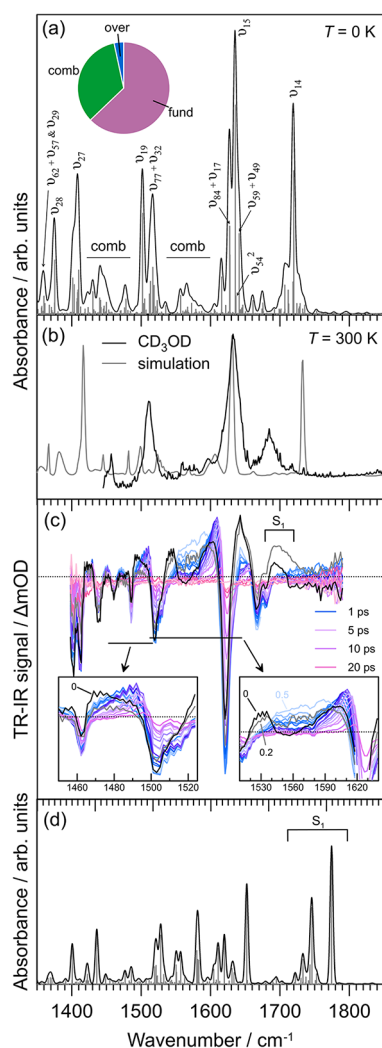


Figure 2. IR and TR-IR spectroscopy of cyan: (a) calculated IR spectrum with 5 cm^{-1} Gaussian convolutions, (b) $T = 300$ K IR spectrum recorded in CD_3OD and MUCA simulated spectrum, (c) TR-IR data following 400 nm excitation in CD_3OD (black [0.0 ps] and gray [0.2 ps] show substantial contributions from the S_1 state), (d) calculated IR spectrum for the S_1 state (VPT2, BH&HLYP/N07D). Note the blue-shifting over the 1700–1800 cm^{-1} range, which is connected with rapid loss of S_1 population and corresponding TR-IR signal in (c).

solvent hydrogen bonding.⁷² Furthermore, some extent of deviation across the entire spectrum is expected due to molecular fluxionality at room temperature, the vibrational Stark effect, and other solute–solvent interactions.^{72,73} Unfortunately, cyan is not soluble in nonpolar solvents, which would best approximate the gas-phase case and provide clearest comparison with theory, so we focus on the ν_{15} mode as it is not strongly coupled with solvent. On the other hand, CD_3OD is a desirable solvent for TR-IR due to an IR-transparent window over the important $\text{C}=\text{C}$ stretching mode; many nonpolar solvents are not suitable for this frequency range.

Experimental TR-IR spectra for cyan in CD_3OD are shown in Figure 2c, showing substantial HGSC band evolution, with the two most important regions highlighted in the inset. It is worth noting that the two shortest pump–probe delays (0 and

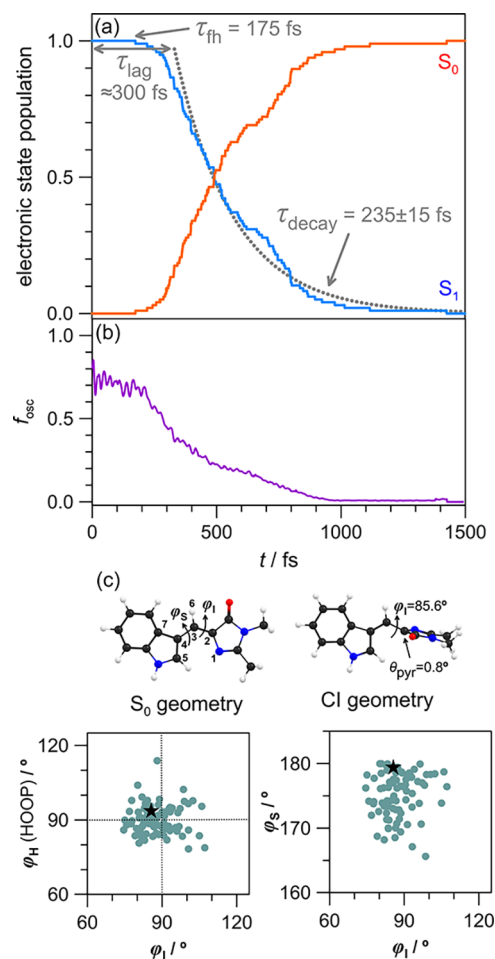


Figure 3. NAMD trajectories for isolated cyan: (a) Evolution of S_1 and S_0 state populations with time. With an initial onset region before dihedral twisting ($\tau_{\text{lag}} \approx 300$ fs and first hop $\tau_{\text{h}} \approx 175$ fs) and an exponential fit to the decay portion of the S_1 state population (lifetime $\tau_{\text{decay}} = 235$ fs), providing the excited state lifetime of $\tau_1 = \tau_{\text{lag}} + \tau_{\text{decay}} = 535$ fs. (b) Evolution of average fluorescence oscillator strength, f_{osc} . (c) Illustration of the S_0 state equilibrium and CI geometries, noting dihedral angles ϕ_1 (1–2–3–4) and ϕ_s (2–3–4–7). The hydrogen-out-of-plane (HOOP) angle is ϕ_H (6–3–4–7). The pyramidalization angle, θ_{pyr} , is defined for the CI geometry. The lower two plots show surface-hopping geometries, with the star representing the optimized minimum energy crossing point (MECP).

0.2 ps) show contributions from IR bands associated with the S_1 electronic state (Figure 2d).³¹

The NAMD trajectories, used to obtain the initial occupation numbers n_i to model HGSC, are summarized in Figure 3a. They provide the $S_1 \rightarrow S_0$ decay lifetime of $\tau_1 = 535$ fs, which is consistent with ultrafast transient absorption measurements at 350 ± 80 fs (ethanol, $\eta = 1.07$ cP) and 580 ± 130 fs (ethylene glycol, $\eta = 16.1$ cP).³¹ The NAMD $Z \rightarrow E$ photoisomerization quantum yield, $\phi_{Z \rightarrow E}$, was 46.4% due to a friction-free environment, and there was no statistical difference in decay lifetime for trajectories forming E vs Z isomers. The average time-dependent fluorescence oscillator strength for all trajectories, f_{osc} in Figure 3b, provides a similar excited state fluorescence lifetime, and is again consistent with femtosecond fluorescence upconversion lifetimes (which agree well with τ_1 lifetimes from transient absorption).³¹ The minimum energy crossing point (MECP, Figure 3c) has a twisted methylene bridge ($\phi_1 = 85.6^\circ$), with the surface

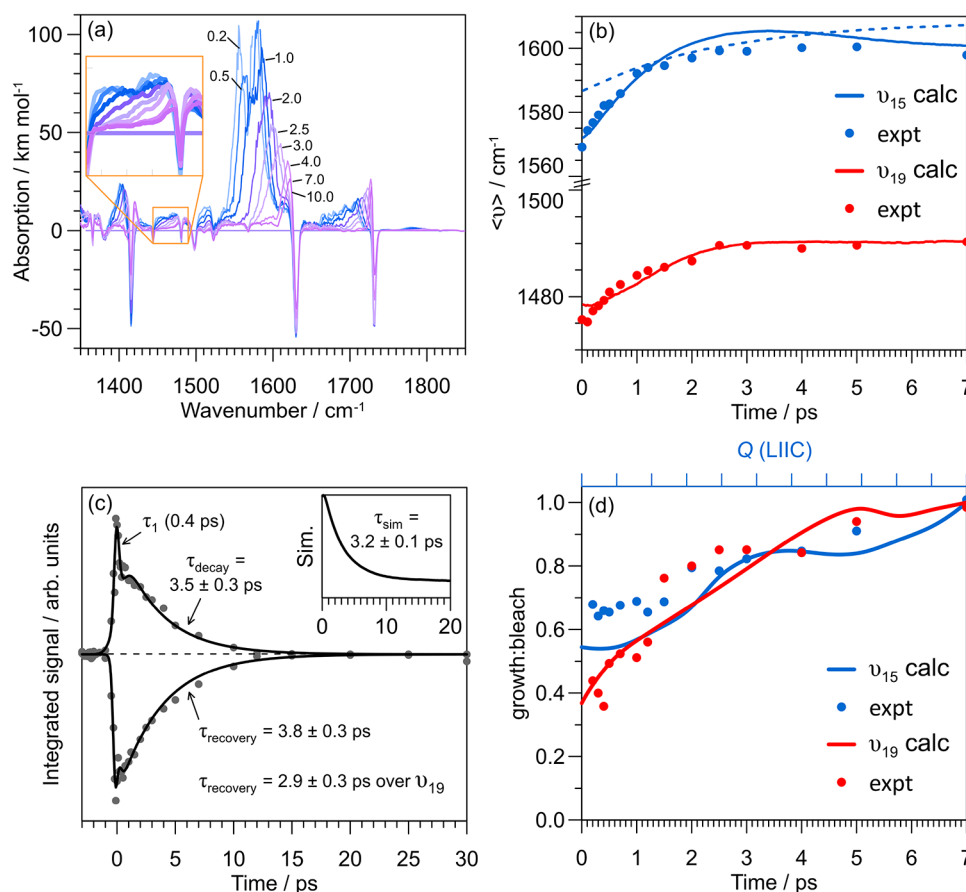


Figure 4. HGSC modeling for cyan: (a) TR-IR spectra over the experimental window modeled using the adjustable parameter $q = 0.1$. The inset shows cooling over ν_{19} . (b) HGSC band expectation frequency, $\langle \nu \rangle$, over the two marker bands; this metric quantifies band reshaping. Experimental data are given as points, modeling using n_i from NAMD trajectories are the solid lines, while the dashed line corresponds to an initial statistical distribution. (c) Experimental HGSC lifetimes derived from numerical integration over the strongest TR-IR bands shown in Figure 2c (centered over ν_{15}). The inset shows the modeled value over the ν_{15} band assuming the same numerical integration range. (d) Calculated (harmonic) change in I , as growth:bleach ratio, for ν_{15} and ν_{19} integration windows with relaxation along the potential energy surface LIIC between the MECP and equilibrium geometry. Experimental data points are taken from numerical integration of growth and depletion bands from insets in Figure 2c.

hopping geometries showing a moderately tight geometric distribution about the CI geometry, and only a small degree of pyramidization, θ_{pyr} of C(2).⁷⁴ Because ϕ_{Z-E} in solution is only a few percent,⁷⁵ surface crossings presumably occur mostly for values of ϕ_1 less than the MECP value; these crossings are localized in the quadrant containing the star in Figure 3c, left.

The simulated TR-IR spectra for cyan are shown in Figure 4a. There are clear HGSC dynamics over the 1550–1600 cm^{-1} range covering the C=C stretch mode ν_{15} , and similar cooling over the 1440–1490 cm^{-1} (ν_{19}) range. It is important to note that these cooling dynamics encapsulate the relevant 1 + 1 combination bands and first overtones along with the fundamental bands, so that the HGSC rates always correlate with multiple modes. To compare with experiment, the expectation time-dependent frequency, $\langle \nu \rangle$, was computed over each HGSC band (Figure 4b), revealing good agreement with experiment. On the other hand, HGSC assuming a statistical vibrational distribution in the rapid exchange limit (but no IVR) gave the dashed line in Figure 4b, which deviates from experiment. Similar agreement is found over the ν_{15} mode, although there are several overlapping modes and a nearby 1 + 1 combination band ($\nu_{77} + \nu_{32}$) that involve heteroatoms that will be strongly coupled with hydrogen-

bonding solvents. In addition, HGSC is evident over the 1650–1730 cm^{-1} range, containing the carbonyl stretch mode (ν_{14}), where solute–solvent hydrogen bonding effect is strong.

Fits to the integrated experimental TR-IR absorption and bleach signals over ν_{15} band to a sequential first-order model, $S_1 \xrightarrow{\tau_1} S_0^* \xrightarrow{\tau_2} S_0$, where τ_2 is τ_{decay} or τ_{recovery} , are shown in Figure 4c. Component τ_1 is linked with decay of the S_1 electronic state.³¹ The HGSC lifetimes from TR-IR are longer than those from transient absorption spectroscopy (e.g., $\tau_2 = 2.5 \pm 0.5$ ps in ethanol),³¹ which is expected because the two techniques probe different aspects of HGSC. Specifically, in transient absorption spectroscopy with a concentration c of electronic ground state absorbing species

$$I_{\text{HGSC}} \propto \langle \sigma(t) \rangle c(t) - \langle \sigma_{300\text{ K}} \rangle [c_{300\text{ K}} - c(t)] \quad (7)$$

where $c_{300\text{ K}} \gg c(t)$. Here, the expectation cross-section for probe absorption $\langle \sigma(t) \rangle$, as approximated by vertical excitation oscillator strength along the LIIC,³¹ decreases near the conical intersection geometry. However, it is normal procedure in the transient absorption community to assume an invariant $\langle \sigma(t) \rangle$. The implication is that transient absorption spectroscopy is more sensitive toward measuring a subpopulation of the cooling hot ground state ensemble. However, TR-IR better

probes the entire HGSC ensemble, but band intensity changes with nuclear coordinate depend on several factors. For example, the simulated HGSC growth feature has more intensity than the corresponding bleach, which contrasts with experiment (Figure 2c). There are several complicating factors that contribute: (i) All trajectories in the HGSC model, using n_i from NAMD trajectories, start at $t = 0$. In the experiment, there will be a distribution of initiation times depending on a convolution of τ_1 and the pump–probe cross-correlation (≈ 200 fs). The consequence is that experimental HGSC transients will be broadened for early t . (ii) TR-IR spectra for photoisomerization reactions can often show more ground-state bleach than corresponding hot ground state absorption (Figure 1b), which is in part due to a changing average dipole moment with molecular distortion from the equilibrium geometry (but still corresponding to the same potential energy surface minimum). Specifically, the absorption intensity, I , for a fundamental mode transition has dependence

$$I_{n_i \rightarrow n_i+1} \propto \left| \left(\frac{\partial \mu}{\partial Q} \right)_{Q=0} \right|^2 \quad (8)$$

where μ is the dipole moment vector and Q is a nuclear coordinate, so that $\mu(Q_0)$ is the permanent dipole at the equilibrium geometry. With increasing Q along the reaction coordinate away from the equilibrium geometry, the variation in μ can be described by the usual expansion

$$\begin{aligned} \mu(Q) \approx & \mu(Q_0) + \mu'(Q_0)(Q - Q_0) \\ & + \frac{1}{2}\mu''(Q_0)(Q - Q_0)^2 + \dots \end{aligned} \quad (9)$$

Increasing Q on the same potential energy surface shifts the expansion point in eq 9 toward higher terms such that first overtones, 1 + 1 combination bands, and symmetry-broken modes become important leading to intensity changes. While the TR-IR data suggest that the effect is only moderate for cyan (Figure 4d), it may be approximated by computing $\mu(Q)$ and Hessian matrices along Q , which involved assuming a linear interpolation (11 points in total) in internal coordinates between the equilibrium and MECP geometries.³¹ The calculated changes for fundamental modes ν_{19} and ν_{15} , which are the major HGSC marker modes in the TR-IR measurements (Figure 2c), are shown in Figure 4d and follow the integrated ratios of the experimental data.

The modeling has no explicit treatment of IVR, rather our expression for $p_{\text{down},i} = qn_i\nu_i dt$ captures the total HGSC process over the experimental TR-IR window (limited by solvent absorption). In principle, IVR is facilitated by anharmonic couplings with low frequency modes acting as doorway modes for IET. The good agreement found for simulated HGSC properties in this work with experiment is because IVR and IET have similar rates. Ideally, measurement of TR-IR data over an extended spectral window, e.g., down to several hundred wavenumbers (experimentally challenging), and in a series of solvents with differing solvent–solute interaction (e.g., with and without hydrogen bonding character, and also changing viscosity), would allow for clearer consideration of IVR.

A key question is how sensitive/unique are the modeled HGSC spectral signatures? While an answer is molecule-specific, depending on each mode and anharmonic constants, there is generally no strong dependence on n_i when varied by a

quantum or so for given mode. This is particularly true when the HGSC transients are complicated by several overlapping modes, such as 1 + 1 combinations bands and fundamentals. Consequently, it is not possible to use experimental HGSC transients to determine details of the photoisomerization mechanism. On the other hand, HGSC modeling would ideally consider an extended spectral range (often limited by the solvent), allowing observation of many active modes, or across multiple solvents. In such a case, analysis should consider also which modes (fundamental and 1 + 1 combination bands) do not show HGSC evolution (i.e., spectator modes) due to low occupation numbers.

CONCLUSIONS

An anharmonic cascade framework for modeling hot ground state cooling in ultrafast photoisomerizing molecules has been reported. This relatively simple model is able to capture properties of HGSC transients for active, marker modes that are not strongly perturbed by solute–solvent interactions. The HGSC framework is readily extendible to similar molecules, such as (barrierless) Z stilbenes, ultrafast photoisomerizing retinals, or E-Z-type molecular photoswitches. Our demonstration on cyan considered a restricted wavelength window due to solvent absorption, where we were able to observe a diagnostic C=C stretch mode linked with the isomerization process. Spectator modes, which are not involved in isomerization, will not show marked HGSC spectral evolution. Because HGSC transients correspond to an averaged response measurement and many combinations (e.g., initial occupation numbers) could lead to similar spectral outcomes, it is difficult to analyze experimental HGSC transients to infer the dynamics that gave rise to the hot ground state. For systems in which IVR is expected to be substantially more rapid than IET, the HGSC dynamics might be better described in the simpler case involving statistical internal energy distributions.

The HGSC framework applied to cyan used a single adjustable parameter, q , linked with the probability for a downward and upward step in n_i . In simple terms, the present IET rates capture a decreasing probability with decreasing n_i but neglects all other mode specificity; in the condensed phase, solvents with strong solute–solvent interactions, notably hydrogen bonding, generally facilitate efficient IET. At present this is the main weakness of the approach; a robust treatment for q is an exceptionally challenging problem depending on many factors, including solvent modes and solvent–solute mode couplings. The HGSC framework as presented can easily accommodate mode-specific q_i , e.g., determined empirically through systematic measurements, removing q as an adjustable variable.

ASSOCIATED CONTENT

Data Availability Statement

The data that support the findings in this work are available from the corresponding authors upon reasonable request.

Supporting Information

The Supporting Information is available free of charge at <https://pubs.acs.org/doi/10.1021/acs.jpcb.5c07581>.

Tabulation of numerical data for anharmonic modes, illustrations of ν_{15} and ν_{19} , and ν_{74} fundamental modes, assignments of fundamental modes, HGSC modeling assuming the rapid exchange limit (PDF)

■ AUTHOR INFORMATION

Corresponding Authors

James N. Bull – Chemistry, Faculty of Science, University of East Anglia, Norwich NR4 7TJ, U.K.; orcid.org/0000-0003-0953-1716; Email: james.bull@uea.ac.uk

Mark H. Stockett – Department of Physics, Stockholm University, SE-10691 Stockholm, Sweden; orcid.org/0000-0003-4603-5172; Email: mark.stockett@fysik.su.se

Authors

Pratip Chakraborty – Chemistry, Faculty of Science, University of East Anglia, Norwich NR4 7TJ, U.K.

Eleanor K. Ashworth – Chemistry, Faculty of Science, University of East Anglia, Norwich NR4 7TJ, U.K.; orcid.org/0000-0003-4805-4860

Anam Fatima – Chemistry, Faculty of Science, University of East Anglia, Norwich NR4 7TJ, U.K.; orcid.org/0000-0003-2388-4390

Vincent J. Esposito – Chemistry, Schmid College of Science and Technology, Chapman University, Orange, California 92866, United States; orcid.org/0000-0001-6035-3869

Gregory M. Greetham – Central Laser Facility, Research Complex at Harwell, Rutherford Appleton Laboratory, Didcot OX11 0QX, U.K.; orcid.org/0000-0002-1852-3403

Partha Malakar – Central Laser Facility, Research Complex at Harwell, Rutherford Appleton Laboratory, Didcot OX11 0QX, U.K.; orcid.org/0000-0001-6874-7010

Stephen R. Meech – Chemistry, Faculty of Science, University of East Anglia, Norwich NR4 7TJ, U.K.; orcid.org/0000-0001-5561-2782

Complete contact information is available at:
<https://pubs.acs.org/10.1021/acs.jpcb.5c07581>

Notes

The authors declare no competing financial interest.

■ ACKNOWLEDGMENTS

This work was funded by an EPSRC New Investigator Award (EP/W018691 to J.N.B.), the Olle Engkvist Foundation (award 200-575 to M.H.S.), and an EPSRC grant (EP/X011410 to S.R.M.). V.J.E. acknowledges support from Chapman University, and acknowledges computer time from the Aiken cluster of the NASA Advanced Supercomputer (NAS). The NAMD part of this work used the ARCHER2 UK National Supercomputing Service (<https://www.archer2.ac.uk>) and the High Performance Computing Cluster (ADA) supported by the Research and Specialist Computing Support service at the University of East Anglia. Prof. Cheol Ho Choi and Woojin Park, Kyungpook National University, are thanked for helpful discussions and guidance on MRSF-TDDFT. Prof. Andrew Orr-Ewing, University of Bristol, is thanked for discussions on TR-IR spectroscopy.

■ REFERENCES

- (1) Levine, B. G.; Martínez, T. J. Isomerization Through Conical Intersections. *Annu. Rev. Phys. Chem.* **2007**, *58*, 613–634.
- (2) Schoenlein, R. W.; Peteanu, L. A.; Mathies, R. A.; Shank, C. V. The First Step in Vision: Femtosecond Isomerization of Rhodopsin. *Science* **1991**, *254*, 412–415.
- (3) Gai, F.; Hasson, K. C.; McDonald, J. C.; Anfinrud, P. A. Chemical Dynamics in Proteins: The Photoisomerization of Retinal in Bacteriorhodopsin. *Science* **1998**, *279*, 1886–1891.
- (4) Andresen, M.; Stiel, A. C.; Trowitzsch, S.; Weber, G.; Eggeling, C.; Wahl, M. C.; Hell, S. W.; Jakobs, S. Structural Basis for Reversible Photoswitching in Dronpa. *Proc. Natl. Acad. Sci. U.S.A.* **2007**, *104*, 13005–13009.
- (5) van Wilderen, L. J. G. W.; van der Horst, M. A.; van Stokkum, I. H. M.; Hellingwerf, K. J.; van Grondelle, R.; Groot, M. L. Ultrafast Infrared Spectroscopy Reveals a Key Step For Successful Entry Into the Photocycle For Photoactive Yellow Protein. *Proc. Natl. Acad. Sci. U.S.A.* **2006**, *103*, 15050–15055.
- (6) Pande, K.; Hutchison, C. D. M.; Groenhof, G.; Aquila, A.; Robinson, J. S.; Tenboer, J.; Basu, S.; Boutet, S.; DePonte, D. P.; Liang, M.; White, T. A.; Zatsepin, N. A.; Yefanov, O.; Morozov, D.; Oberthuer, D.; Gati, C.; Subramanian, G.; James, D.; Zhao, Y.; Koralek, J.; Brayshaw, J.; Kupitz, C.; Conrad, C.; Roy-Chowdhury, S.; Coe, J. D.; Metz, M.; Xavier, P. L.; Grant, T. D.; Koglin, J. E.; Ketawala, G.; Fromme, R.; Šrajer, V.; Henning, R.; Spence, J. C. H.; Ourmazd, A.; Schwander, P.; Weierstall, U.; Frank, M.; Fromme, P.; Barty, A.; Chapman, H. N.; Moffat, K.; van Thor, J. J.; Schmidt, M. Femtosecond Structural Dynamics Drives the *trans/cis* Isomerization in Photoactive Yellow Protein. *Protein Sci.* **2016**, *352*, 725–729.
- (7) *Molecular Switches*, 2nd ed.; Feringa, B. L.; Browne, W. R., Eds.; Wiley-VCH: Weinheim, Germany, 2011.
- (8) van Leeuwen, T.; Lubbe, A. S.; Stacko, P.; Wezenberg, S. J.; Feringa, B. L. Dynamic Control of Function by Light-Driven Molecular Motors. *Nat. Rev. Chem.* **2017**, *1*, No. 0096.
- (9) Roke, D.; Wezenberg, S. J.; Feringa, B. L. Molecular Rotary Motors: Unidirectional Motion Around Double Bonds. *Proc. Natl. Acad. Sci. U.S.A.* **2018**, *115*, 9423–9431.
- (10) García-López, V.; Liu, D.; Tour, J. M. Light-Activated Organic Molecular Motors and Their Applications. *Chem. Rev.* **2020**, *120*, 79–124.
- (11) Roy, P.; Sardjan, A. S.; Browne, W. R.; Feringa, B. L.; Meech, S. R. Excited State Dynamics in Unidirectional Photochemical Molecular Motors. *J. Am. Chem. Soc.* **2024**, *146*, 12255–12270.
- (12) Schultz, T.; Quenneville, J.; Levine, B.; Toniolo, A.; Martínez, T. J.; Lochbrunner, S.; Schmitt, M.; Shaffer, J. P.; Zgierski, M. Z.; Stolow, A. Mechanism and Dynamics of Azobenzene Photoisomerization. *J. Am. Chem. Soc.* **2003**, *125*, 8098–8099.
- (13) Elles, C. G.; Crim, F. F. Connecting Chemical Dynamics in Gases and Liquids. *Annu. Rev. Phys. Chem.* **2006**, *57*, 273–302.
- (14) Balevičius Jr, V., Jr.; Wei, T.; Di Tommaso, D.; Abramavicius, D.; Hauer, J.; Polívka, T.; Duffy, C. D. P. The Full Dynamics of Energy Relaxation in Large Organic Molecules: From Photo-Excitation to Solvent Heating. *Chem. Sci.* **2019**, *10*, 4792–4804.
- (15) Owrutsky, J. C.; Raftery, D.; Hochstrasser, R. M. Vibrational Relaxation Dynamics in Solutions. *Annu. Rev. Phys. Chem.* **1994**, *45*, 519–555.
- (16) Bigwood, R.; Gruebele, M.; Leitner, D. M.; Wolynes, P. G. The Vibrational Energy Flow Transition in Organic Molecules. *Proc. Natl. Acad. Sci. U.S.A.* **1998**, *95*, 5960–5964.
- (17) Grubb, M. P.; Coulter, P. M.; Marroux, H. J. B.; Orr-Ewing, A. J.; Ashfold, M. N. R. Unravelling the Mechanisms of Vibrational Relaxation in Solution. *Chem. Sci.* **2017**, *8*, 3062–3069.
- (18) Ventura, E.; Andrade do Monte, S.; T do Casal, M.; Pinheiro, M.; Toldo, J. M.; Barbatti, M. Modeling the Heating and Cooling of a Chromophore After Photoexcitation. *Phys. Chem. Chem. Phys.* **2022**, *24*, 9403–9410.
- (19) Skinner, J. L. Vibrational Energy Relaxation of Small Molecules and Ions in Liquids. *Theor. Chem. Acc.* **2011**, *128*, 147–155.
- (20) Aßmann, J.; Kling, M.; Abel, B. Watching Photoinduced Chemistry and Molecular Energy Flow in Solution in Real Time. *Angew. Chem., Int. Ed.* **2003**, *42*, 2226–2246.
- (21) Yamada, Y.; Katsumoto, Y.; Ebata, T. Picosecond IR-UV Pump-Probe Spectroscopic Study on the Vibrational Energy Flow in Isolated Molecules and Clusters. *Phys. Chem. Chem. Phys.* **2007**, *9*, 1170–1185.
- (22) Hanes, A. T.; Grieco, C.; Lalis, R. F.; Hadad, C. M.; Kohler, B. Vibrational Relaxation by Methylated Xanthenes in Solution:

Insights From 2D IR Spectroscopy and Calculations. *J. Chem. Phys.* **2023**, *158*, No. 044302, DOI: 10.1063/5.0135412.

(23) Sension, R. J.; Szarka, A. Z.; Hochstrasser, R. M. Vibrational Energy Redistribution and Relaxation in the Photoisomerization of *Cis*-Stilbene. *J. Chem. Phys.* **1992**, *97*, 5239–5242.

(24) Sension, R. J.; Repinec, S. T.; Szarka, A. Z.; Hochstrasser, R. M. Femtosecond Laser Studies of the *Cis*-Stilbene Photoisomerization Reactions. *J. Chem. Phys.* **1993**, *98*, 6291–6315.

(25) Phillips, D. L.; Rodier, J.-M.; Myers, A. B. *Cis*-stilbene Photochemistry: Direct Observation of Product Formation and Relaxation Through Two-Color UV Pump-Probe Raman Spectroscopy. *Chem. Phys.* **1993**, *175*, 1–12.

(26) Cox, M. J.; Crim, F. F. Vibrational Energy Flow Rates for *Cis*- and *Trans*-Stilbene Isomers in Solution. *J. Phys. Chem. A* **2005**, *109*, 11673–11678.

(27) Briney, K. A.; Herman, L.; Boucher, D. S.; Dunkelberger, A. D.; Crim, F. F. The Influence of Vibrational Excitation on the Photoisomerization of *Trans*-Stilbene in Solution. *J. Phys. Chem. A* **2010**, *114*, 9788–9794.

(28) Shelby, R. M.; Harris, C. B.; Cornelius, P. A. The Origin of Vibrational Dephasing of Polyatomic Molecules in Condensed Phases. *J. Chem. Phys.* **1979**, *70*, 34–41.

(29) Hamm, P.; Ohline, S. M.; Zinth, W. Vibrational Cooling After Ultrafast Photoisomerization of Azobenzene Measured by Femtosecond Infrared Spectroscopy. *J. Chem. Phys.* **1997**, *106*, 519–529.

(30) Murdock, D.; Harris, S. J.; Luke, J.; Grubb, M. P.; Orr-Ewing, A. J.; Ashfold, M. N. R. Transient UV Pump-IR Probe Investigation of Heterocyclic Ring-Opening Dynamics in the Solution Phase: The Role Played by $\pi\sigma^*$ States in the Photoinduced Reactions of Thiophenone and Furanone. *Phys. Chem. Chem. Phys.* **2014**, *16*, 21271–21279.

(31) Fatima, A.; Ashworth, E. K.; Chambrier, I.; Cammidge, A. N.; Bressan, G.; Meech, S. R.; Bull, J. N. Ultrafast Photophysics of the Cyan Fluorescent Protein Chromophore in Solution. *Phys. Chem. Chem. Phys.* **2025**, *27*, 9407–9416.

(32) Barone, V. Anharmonic Vibrational Properties by a Fully Automated Second-Order Perturbative Approach. *J. Chem. Phys.* **2004**, *122*, No. 014108.

(33) Berg, B. A. Multicanonical Recursions. *J. Stat. Phys.* **1996**, *82*, 323–342.

(34) Berg, B. A. Multicanonical Simulations Step by Step. *Comput. Phys. Commun.* **2003**, *153*, 397–406.

(35) Hastings, W. K. Monte Carlo Sampling Methods Using Markov Chains and Their Applications. *Biometrika* **1970**, *57*, 97–109.

(36) Stein, S. E.; Rabinovitch, B. S. Accurate Evaluation of Internal Energy Level Sums and Densities Including Anharmonic Oscillators and Hindered Rotors. *J. Chem. Phys.* **1973**, *58*, 2438–2445.

(37) Wang, F.; Landau, D. P. Efficient, Multiple-Range Random Walk Algorithm to Calculate the Density of States. *Phys. Rev. Lett.* **2001**, *86*, 2050–2053.

(38) Becke, A. D. A New Mixing of Hartree-Fock and Local Density-Functional Theories. *J. Chem. Phys.* **1993**, *98*, 1372–1377.

(39) Barone, V.; Cimino, P.; Stendardo, E. Development and Validation of the B3LYP/N07D Computational Model for Structural Parameter and Magnetic Tensors of Large Free Radicals. *J. Chem. Theory Comput.* **2008**, *4*, 751–764.

(40) Frisch, M. J.; Trucks, G. W.; Schlegel, H. B.; Scuseria, G. E.; Robb, M. A.; Cheeseman, J. R.; Scalmani, G.; Barone, V.; Mennucci, B.; Petersson, G. A.; Nakatsuji, H.; Caricato, M.; Li, X.; Hratchian, H. P.; Izmaylov, A. F.; Bloino, J.; Zheng, G.; Sonnenberg, J. L.; Hada, M.; Ehara, M.; Toyota, K.; Fukuda, R.; Hasegawa, J.; Ishida, M.; Nakajima, T.; Honda, Y.; Kitao, O.; Nakai, H.; Vreven, T.; Montgomery, J. A., Jr.; Peralta, J. E.; Ogliaro, F.; Bearpark, M.; Heyd, J. J.; Brothers, E.; Kudin, K. N.; Staroverov, V. N.; Kobayashi, R.; Normand, J.; Raghavachari, K.; Rendell, A.; Burant, J. C.; Iyengar, S. S.; Tomasi, J.; Cossi, M.; Rega, N.; Millam, J. M.; Klene, M.; Knox, J. E.; Cross, J. B.; Bakken, V.; Adamo, C.; Jaramillo, J.; Gomperts, R.; Stratmann, R. E.; Yazyev, O.; Austin, A. J.; Cammi, R.; Pomelli, C.; Ochterski, J. W.; Martin, R. L.; Morokuma, K.; Zakrzewski, V. G.;

Voth, G. A.; Salvador, P.; Dannenberg, J. J.; Dapprich, S.; Daniels, A. D.; Farkas, Ö.; Foresman, J. B.; Ortiz, J. V.; Cioslowski, J.; Fox, D. J. *Gaussian 16 Revision B.01*. Gaussian Inc.: Wallingford, CT, 2016.

(41) Barone, V.; Biczysko, M.; Bloino, J. Fully Anharmonic IR and Raman Spectra of Medium-Size Molecular Systems: Accuracy and Interpretation. *Phys. Chem. Chem. Phys.* **2014**, *16*, 1759–1787.

(42) Mackie, C. J.; Candian, A.; Huang, X.; Lee, T. J.; Tielens, A. G. M. Linear Transformation of Anharmonic Molecular Force Constants Between Normal and Cartesian Coordinates. *J. Chem. Phys.* **2015**, *142*, 244107.

(43) Mills, I. *Molecular Spectroscopy: Modern Research*; Rao, N.; Mathews, C. W., Eds.; Academic Press: New York, 1972.

(44) Watson, J. K. G. *Vibrational Spectra and Structure*; Daring, J. R., Ed.; Elsevier, 1977; pp 1–89.

(45) Papoušek, D.; Aliey, M. R. *Molecular Vibration-Rotation Spectra*; Elsevier: Amsterdam, 1982.

(46) Gaw, J. F.; Willets, A.; Green, W. H.; Handy, N. C. *Advances in Molecular Vibrations and Collision Dynamics*; Bowman, J. M.; Ratner, M. A., Eds.; JAI Press, Inc., 1991; pp 170–185.

(47) Martin, J. M. L.; Taylor, P. R. Accurate Ab Initio Quartic Force Field for *trans*-HNNH and Treatment of Resonance Polyads. *Spectrochim. Acta, A* **1997**, *53*, 1039–1050.

(48) Martin, J. M. L.; Lee, T. J.; Taylor, P. R.; François, J.-P. The Anharmonic Force Field of Ethylene, C_2H_4 , by Means of Accurate Ab Initio Calculations. *J. Chem. Phys.* **1995**, *103*, 2589–2602.

(49) Mackie, C. J.; Candian, A.; Huang, X.; Maltseva, E.; Petrignani, A.; Oomens, J.; Buma, W. J.; Lee, T. J.; Tielens, A. G. G. M. The Anharmonic Quartic Force Field Infrared Spectra of Three Polycyclic Aromatic Hydrocarbons: Naphthalene, Anthracene, and Tetracene. *J. Chem. Phys.* **2015**, *143*, No. 224314, DOI: 10.1063/1.4936779.

(50) Esposito, V. J.; Fortenberry, R. C.; Boersma, C.; Allamandola, L. J. Assigning the CH Stretch Overtone Spectrum of Benzene and Naphthalene with Extension to Anthracene and Tetracene Using 2- and 3-quanta Anharmonic Quantum Chemical Computations. *J. Chem. Phys.* **2024**, *160*, No. 211101, DOI: 10.1063/5.0208597.

(51) Esposito, V. J.; Allamandola, L. J.; Boersma, C.; Bregman, J. D.; Fortenberry, R. C.; Maragkoudakis, A.; Temi, P. Anharmonic IR Absorption Spectra of the Prototypical Interstellar PAHs Phenanthrene, Pyrene, and Pentacene in Their Neutral and Cation States. *Mol. Phys.* **2023**, *122*, No. 2252936, DOI: 10.1080/00268976.2023.2252936.

(52) Douglas-Walker, T. E.; Ashworth, E. K.; Stockett, M. H.; Daly, F. C.; Chambrier, I.; Esposito, V. J.; Gerlach, M.; Zheng, A.; Palotás, J.; Cammidge, A. N.; Campbell, E. K.; Brünken, S.; Bull, J. N. Vibrational and Electronic Spectroscopy of 2-Cyanoindene Cations. *ACS Earth Space Chem.* **2025**, *9*, 134–145.

(53) Stockett, M. H.; Esposito, V. J.; Ashworth, E. K.; Jacovella, U.; Bull, J. N. Infrared Cooling in an Anharmonic Cascade Framework: 2-Cyanoindene, the Smallest Cyano-PAH Identified in Taurus Molecular Cloud-1. *ACS Earth Space Chem.* **2025**, *9*, 382–393.

(54) Laurent, A. D.; Jacquemin, D. TD-DFT benchmarks: A review. *Int. J. Quantum Chem.* **2013**, *113*, 2019–2039.

(55) Lee, S.; Park, W.; Choi, C. H. Expanding Horizons in Quantum Chemical Studies: The Versatile Power of MRSF-TDDFT. *Acc. Chem. Res.* **2025**, *58*, 208–217.

(56) Francl, M. M.; Pietro, W. J.; Hehre, W. J.; Binkley, J. S.; Gordon, M. S.; DeFrees, D. J.; Pople, J. A. Self-Consistent Molecular Orbital Methods. XXIII. A Polarization-Type Basis Set for Second-Row Elements. *J. Chem. Phys.* **1982**, *77*, 3654–3665.

(57) Barca, G. M. J.; Bertoni, C.; Carrington, L.; Datta, D.; De Silva, N.; Deustua, J. E.; Fedorov, D. G.; Gour, J. R.; Gunina, A. O.; Guidez, E.; Harville, T.; Irle, S.; Ivanic, J.; Kowalski, K.; Leang, S. S.; Li, H.; Li, W.; Lutz, J. J.; Magoulas, I.; Mato, J.; Mironov, V.; Nakata, H.; Pham, B. Q.; Piecuch, P.; Poole, D.; Pruitt, S. R.; Rendell, A. P.; Roskop, L. B.; Ruedenberg, K.; Sattasathuchana, T.; Schmidt, M. W.; Shen, J.; Slipchenko, L.; Sosonkina, M.; Sundriyal, V.; Tiwari, A.; Galvez Vallejo, J. L.; Westheimer, B.; Wloch, M.; Xu, P.; Zahariev, F.; Gordon, M. S. Recent Developments in the General Atomic and

- Molecular Electronic Structure System. *J. Chem. Phys.* **2020**, *152*, No. 154102.
- (58) Tully, J. C. Molecular Dynamics With Electronic Transitions. *J. Chem. Phys.* **1990**, *93*, 1061–1071.
- (59) Lee, S.; Kim, E.; Lee, S.; Choi, C. H. Fast Overlap Evaluations for Nonadiabatic Molecular Dynamics Simulations: Applications to SF-TDDFT and TDDFT. *J. Chem. Theory Comput.* **2019**, *15*, 882–891.
- (60) Lee, S.; Horbatenko, Y.; Filatov, M.; Choi, C. H. Fast and Accurate Computation of Nonadiabatic Coupling Matrix Elements Using the Truncated Leibniz Formula and Mixed-Reference Spin-Flip Time-Dependent Density Functional Theory. *J. Phys. Chem. Lett.* **2021**, *12*, 4722–4728.
- (61) Mitrić, R.; Werner, U.; Bonačić-Koutecký, V. Nonadiabatic Dynamics and Simulation of Time Resolved Photoelectron Spectra Within Time-Dependent Density Functional Theory: Ultrafast Photoswitching in Benzylideneaniline. *J. Chem. Phys.* **2008**, *129*, No. 164118.
- (62) Park, W.; Oh, J.; Kim, J.; Lee, S.; Kim, J. H.; Huix-Rotllant, M.; Kim, D.; Choi, C. H. Temperature Controlled Decay and Pendulum Dynamics of Green Fluorescent Protein (GFP) Chromophore. *J. Phys. Chem. Lett.* **2024**, *15*, 11468–11475.
- (63) Huix-Rotllant, M.; Park, W.; Mazaherifar, M.; Choi, C. H. Assessing Spin-Flip Time-Dependent Density-Functional-Based Tight-Binding for Describing Z/E Photoisomerization Reactions. *Theor. Chem. Acc.* **2025**, *144*, 41.
- (64) Ceriotti, M.; Bussi, G.; Parrinello, M. Langevin Equation with Colored Noise for Constant-Temperature Molecular Dynamics Simulations. *Phys. Rev. Lett.* **2009**, *102*, No. 020601.
- (65) Ceriotti, M.; Bussi, G.; Parrinello, M. Colored-Noise Thermostats à la Carte. *J. Chem. Theory Comput.* **2010**, *6*, 1170–1180.
- (66) Hollas, D.; Suchan, J.; Onćčák, M.; Svoboda, O.; Slavíček, P. ABIN. <https://github.com/PHOTOX/ABIN> (accessed Aug 15, 2025).
- (67) GLE4MD. GLE4MD Project. <http://gle4md.org/> (accessed Sept 2, 2025).
- (68) Prlj, A.; Hollas, D.; Curchod, B. F. E. Deciphering the Influence of Ground-State Distributions on the Calculation of Photolysis Observables. *J. Phys. Chem. A* **2023**, *127*, 7400–7409.
- (69) Greetham, G. M.; Burgos, P.; Cao, Q.; Clark, I. P.; Codd, P. S.; Farrow, R. C.; George, M. W.; Kogimtzis, M.; Matousek, P.; Parker, A. W.; Pollard, M. R.; Robinson, D. A.; Xin, Z.-J.; Towrie, M. Ultra: A Unique Instrument for Time-Resolved Spectroscopy. *Appl. Spectrosc.* **2010**, *64*, 1311–1319.
- (70) Merrick, J. P.; Moran, D.; Radom, L. An Evaluation of Harmonic Vibrational Frequency Scale Factors. *J. Phys. Chem. A* **2007**, *111*, 11683–11700.
- (71) Ramakrishnan, R.; Rauhut, G. Semi-Quartic Force Fields Retrieved From Multi-Mode Expansions: Accuracy, Scaling Behavior, and Approximations. *J. Chem. Phys.* **2015**, *142*, 154118.
- (72) Schneider, S. H.; Kratochvil, H. T.; Zanni, M. T.; Boxer, S. G. Solvent-Independent Anharmonicity for Carbonyl Oscillators. *J. Phys. Chem. B* **2017**, *121*, 2331–2338.
- (73) Baiz, C. R.; Blasiak, B.; Bredenbeck, J.; Cho, M.; Choi, J.-H.; Corcelli, S. A.; Dijkstra, A. G.; Feng, C.-J.; Garrett-Roe, S.; Ge, N.-H.; Hanson-Heine, M. W. D.; Hirst, J. D.; Jansen, T. L. C.; Kwac, K.; Kubarych, K. J.; Londergan, C. H.; Maekawa, H.; Reppert, M.; Saito, S.; Roy, S.; Skinner, J. L.; Stock, G.; Straub, J. E.; Thielges, M. C.; Tominaga, K.; Tokmakoff, A.; Torii, H.; Wang, L.; Webb, L. J.; Zanni, M. T. Vibrational Spectroscopic Map, Vibrational Spectroscopy, and Intermolecular Interaction. *Chem. Rev.* **2020**, *120*, 7152–7218.
- (74) Conyard, J.; Heisler, I. A.; Chan, Y.; Bulman Page, P. C.; Meech, S. R.; Blancafort, L. A New Twist in the Photophysics of the GFP Chromophore: A Volume-Conserving Molecular Torsion Couple. *Chem. Sci.* **2018**, *9*, 1803–1812.
- (75) Voliani, V.; Bizzarri, R.; Nifosi, R.; Abbruzzetti, S.; Grandi, E.; Viappiani, C.; Beltram, F. Cis-Trans Photoisomerization of Fluorescent-Protein Chromophores. *J. Phys. Chem. B* **2008**, *112*, 10714–10722.



CAS BIOFINDER DISCOVERY PLATFORM™

CAS BIOFINDER HELPS YOU FIND YOUR NEXT BREAKTHROUGH FASTER

Navigate pathways, targets, and
diseases with precision

Explore CAS BioFinder

